Effect of Cr substitution in ZnFe2O4 nanoparticles on the electron transfer at electrochemical interfaces

Materials Research Bulletin 183 (2025) 113191

Contents lists available at ScienceDirect

Materials Research Bulletin

journal homepage: www.elsevier.com/locate/matresbu

Research Papers

Effect of Cr substitution in $ZnFe_2O_4$ nanoparticles on the electron transfer at electrochemical interfaces

Mallikarjun Madagalam [a,b,c,*], Mattia Bartoli [c,d], Michele Rosito [a], Nicola Blangetti [a], Marco Etzi [d], Elisa Padovano [a,c], Barbara Bonelli [a,c], Sandro Carrara [b], Alberto Tagliaferro [a,c,e]

[a] Department of Applied Science and Technology, Politecnico di Torino, Duca degli Abruzzi 24, Torino 10129, Italy
[b] Bio/CMOS Interfaces Laboratory, École Polytechnique Fédérale de Lausanne, Rue de la Maladière 71b, Neuchâtel CH-2002, Switzerland
[c] National Interuniversity Consortium of Materials Science and Technology Unit of Torino – Politecnico di Torino, Via Giuseppe Giusti, 9, Florence 50121, Italy
[d] Center for Sustainable Future Technologies, Fondazione Istituto Italiano di Tecnologia, Via Livorno 60, Torino 10144, Italy
[e] Faculty of Science, OntarioTechU, 2000 Simcoe Street North, Oshawa, Ontario L1G 0C5, Canada

ARTICLE INFO

Keywords:
Nanomaterials
Ferrite
Chromite
Energy gap
Electron transfer
Paracetamol

ABSTRACT

In this study, we explored the effect of Cr^{3+} substitution by partially and fully replacing Fe^{3+} in the normal spinel $ZnFe_2O_4$ crystal structure at electrochemical interfaces. The resulting $ZnCr_xFe_{2-x}O_4$ nanomaterials exhibited an average particle size between 20 and 50 nm with a spherical morphology. The materials also demonstrated energy band gaps ranging from 2.1 to 3.1 eV X-ray diffraction (XRD) analysis confirmed that all the synthesized materials maintained a normal spinel structure, attributed to the octahedral site preference energy (OSPE) of Zn^{2+}, Fe^{3+}, and Cr^{3+} ions. Electrochemical performance assessments revealed that the $ZnFe_2O_4$-based sensor achieved a sensitivity of (37.8 ± 0.2) μA/mM with a kinetic rate constant of (13.1 ± 2.8) ms^{-1}, while the $ZnCr_2O_4$-based sensor exhibited a sensitivity of (32.4 ± 0.5) μA/mM and a kinetic rate constant of (3.73 ± 0.55) ms^{-1} in the detection of paracetamol, whereas $ZnCrFeO_4$ sensor has produced the second-best sensitivity (35.7 ± 0.1 μA/mM) and the rate constant (4.53 ± 0.54 ms^{-1}) with the lowest limit of detection (1.94 ± 0.01 μM). These differences in electrochemical performance were correlated with the variations in the energy band gaps caused by the restructuring of the normal spinel structure. Our findings indicate that the $ZnFe_2O_4$ sensor has a higher potential for direct electron transfer, whereas the other sensors are more likely to facilitate surface-mediated electron transfer.

1. Introduction

Spinel oxide-based nanomaterials have gained significant attention in the field of nanoscience offering a wide range of applications due to their unique magnetic, electrical, and structural properties [1–3]. The spinel oxide's structure has a face-centered cubic (FCC) arrangement of oxygen anions, with different metal cations occupying tetrahedral (Td) and octahedral (Oh) sites within the lattice [4]. This unique crystal structure provides spinel oxides with interesting magnetic and electrical properties [5,6]. Another key feature of spinel oxides is the ability to form solid solutions with other spinel oxides offering the ability to easily tune their composition, lattice structure, and band gap leading the way for a wide range of applications [7–10]. Spinels can be normal, inverse, or mixed depending on the combination of the trivalent and bivalent cations and their preferential occupancy either of 'Td' or 'Oh' sites. A spinel is defined as normal when bivalent and trivalent cations occupy 'Td' and 'Oh' sites, respectively (eg: $ZnFe_2O_4$, $ZnCr_2O_4$), inverse when 'Oh' sites are shared between trivalent and divalent cations while "Td' sites are occupied by trivalent cations (eg: $NiFe_2O_4$, Fe_3O_4, $CoFe_2O_4$). A spinel is termed mixed when both sites are shared by bivalent and trivalent cations; this latter phase is possible usually when we have solid solutions of normal and inverse spinel oxides (eg: $Zn_{0.4}Ni_{0.6}Fe_2O_4$) [7].

Spinel oxide-based nanomaterials are produced by different techniques, the choice being based on the requirements of the specific application and properties. The two routes of synthesis are: dry synthesis and wet synthesis. Dry synthesis includes solvent-free conventional [7] and microwave-assisted combustion techniques [11]. Wet synthesis techniques include sol-gel [12,13], co-precipitation [14], solvent deficient [15], solvothermal/hydrothermal [16,17], sonochemical methods [18,19]. Sol-gel technique is widely used as size and shape of the

* Corresponding author at: Department of Applied Science and Technology, Politecnico di Torino, Duca degli Abruzzi 24, Torino 10129, Italy.
E-mail address: mallikarjun.madagalam@polito.it (M. Madagalam).

https://doi.org/10.1016/j.materresbull.2024.113191
Received 4 July 2024; Received in revised form 24 October 2024; Accepted 10 November 2024
Available online 12 November 2024

nanoparticles control is possible with different surfactants enhancing different properties of the particles [12,20,21].

Among the large class of spinel nanomaterials, $ZnFe_2O_4$ [7,22] and $ZnCr_2O_4$ [23,24] offer a wide range of possibilities due to their normal spinel lattice structure. Both possess n-type semiconducting nature due to their normal spinel lattice structure as the conductivity is mainly by electron hopping within the crystal sites [7]. Zinc chromite shows wide band energy gap above 3 eV [24,25] whereas zinc ferrite possesses an energy gap around 2.5 eV [7,22], it is found that the band gap energy is a crucial parameter in electrochemical sensing that can impact the electron transfer at the electrochemical interface in our previous work [7, 22]. Zinc ferrite shows ferromagnetic [26] nature (electron hopping in the direction of the electric field) while zinc chromite acts as antiferromagnetic [24] (electron hopping in the opposite direction of the electric field) due to frustrated electron spin. The electron hopping gets affected by the magnetic nature of the materials changing the conductivity [27]. Due to these similar properties, zinc ferrite and zinc chromite are very interesting to study in electrochemical detection.

In electrochemical sensing, zinc ferrite nanomaterials are used as sensing materials in sensing different molecules such as dopamine [28], hydrogen peroxide [5,16,29], heavy metals, and glucose [30,31]. Recently, zinc ferrite and nickel ferrite nanomaterials are deeply investigated for electrochemical sensing of paracetamol [7] and normal spinel $ZnFe_2O_4$ is found to be the best sensor with high sensitivity 'S' and kinetic rate constant 'k'. A comparative study on electrochemical activity of $ZnCr_2O_4$, $ZnCrFeO_4$, $ZnFe_2O_4$, $ZnBiFeO_4$, $ZnBi_2O_4$ [32], and $ZnCr_{2-x}Fe_xO_4$ ($x = 1, 1.25, 1.5, 1.75, 2$) [33] also showed that $ZnFe_2O_4$ is the best sensor for paracetamol sensing. Zinc chromite is used in electrochemical sensing of carcinogenic drugs [34], CO [35], and dopamine and ascorbic acid [36].

From Marcus theory [37,38] and the generalized Marcus theory of electron transfer by Tachiya and Murata [39], electron transfer rate constant 'k' depends on the reorganization energy 'λ' and the transfer integral 'J'. In turn 'λ' and 'J' depend on the ionic radii of the donor and acceptor, and the distance between the donor and acceptor. These parameters can be affected by the size, geometry, crystal structure, and composition of the electrode material. Based on that, in our previous work, we studied the effect of crystal structure ($Zn_xNi_{1-x}Fe_2O_4$) [7] and of larger ionic size by inserting Bi^{3+} into the crystal structure of $ZnFe_2O_4$ ($ZnBi_xFe_{2-x}O_4$) [22] and found that normal spinel $ZnFe_2O_4$ was performing better in terms of sensitivity and rate constant. The aim of this work is to study the effect of similar ionic size by replacing Fe^{3+} with Cr^{3+} partially and fully in $ZnFe_2O_4$ on electron transfer at the electrochemical interface with paracetamol as a test probe molecule. Synthesized nanomaterials ($ZnCr_xFe_{2-x}O_4$) by auto combustion method are characterized to understand the chemical, structural, morphological features. Energy band gap, valence band maximum, and conduction band minimum energies of the nanomaterials are reported. Electrochemical characterization in terms of sensitivity, limit of detection, and rate constant is presented and correlated with the chemical features of the electrode materials. Insights into the electron transfer at the electrochemical interface and the effect of surface states in electrochemical sensing activity are presented and discussed.

2. Materials and methods

2.1. Chemicals

$Zn(NO_3)_2{\bullet}6H_2O$, $Fe(NO_3)_3{\bullet}9H_2O$, $Cr(NO_3)_3{\bullet}9H_2O$, $C(NH_2)_2O$ (Urea), $C_4H_{10}O$ (Butanol), and paracetamol powder are purchased from Sigma Aldrich and used without further purification.

2.2. Material synthesis

Adopted from the literature, auto-combustion method is used for nanomaterial synthesis [7,11]. A redox mixture (1:1 mole ratio) of metal nitrates (oxidizing agents) and urea (reducing agent or fuel) is prepared in a crucible and followed the same procedure as reported previously [7]. The final product is grounded to fine powders of $ZnCr_xFe_{2-x}O_4$ ($x = 0, 0.25, 0.5, 0.75, 1, 2$).

2.3. Physicochemical characterization

Field emission scanning electron microscopy (FESEM Zeiss SupraTM 50, Oberkochen, Germany) is used to analyze the nanomaterials morphology. Micro-Raman spectroscopic measurements are performed (Renishaw, inVia Raman Microscope) to find out the molecular vibrations of the materials. X-ray powder diffraction (PANalytical Empyrean diffractometer (Malvern Panalytical, Malvern, UK)) is used for phases and crystal structure identification with Bragg-Brentano configuration at room temperature and Cu Kα ($\lambda = 1.5418$Å) radiation at 40 kV and 40 mA is used. The analysis is performed in a 2θ range between 10° and 70°, with a step size of 0.013°/s and a time step of 60 s. UV–Visible experiments are performed on a Cary 5000 UV–Vis-NIR spectrophotometer (Varian Instruments, Mulgrave, Australia) equipped with a DR (Diffuse reflectance) apparatus. X-ray photoelectron spectroscopy (XPS) measurements are conducted on a PHI 5000 Versaprobe spectrometer using a monochromatic Al Kα (1486.6 eV) X-ray source. An electron gun and an ion gun are used as a charge compensation system. Binding energy calibration is applied by setting the position of the adventitious sp^3 carbon component at 284.8 eV Pass energies are set at 187.85 and 23.5 eV for the acquisition of survey and high-resolution spectra, respectively. The spectra are processed using CasaXPS software (v2.3.23, Casa Software Ltd).

2.4. Electrodes modification

Screen-printed electrodes (SPE) with carbon working electrode (WE) (area 0.12 cm^2), carbon counter electrode (CE), and Ag/AgCl reference electrode (RE) are used as electrochemical sensing elements. Nanomaterial suspensions are prepared by adding 3 mg material in 1 mL (3:1 material to solvent ratio) of 1-butanol and the solution is put in an ultrasonic bath until it becomes a homogeneous solution. SPEs are modified by spreading 5 μL of nanomaterial suspension on top of the WE and dried overnight (drop-casting technique) **for 24 h** at room temperature.

2.5. Electrochemical measurements

Cyclic voltammetry (CV) is performed by using a Bio-logic SP-300 potentiostat with surface-modified SPEs as electrochemical sensors to sense 4 mM Ferri/Ferrocyanide redox couple in 0.1 M PB (phosphate buffer) at pH 7. Cyclic voltammograms are recorded by dropping 100 μL of electrolytic solution on top of the electrochemical sensor. The potential is applied from −0.4 to 0.8 V (versus Ag/AgCl) at scan rate of 100 mV/s, and the scan rate analysis is performed by changing the scan rate from 25 mV/s to 150 mV/s in steps of 25 mV/s. Electrochemical impedance spectroscopic measurements are conducted in the frequency range from 0.1 – 100 kHz with 10 points per decade at a potential amplitude of 5 mV. After the initial measrements, CV is executed to detect paracetamol in 0.1 M PB at pH 7. The sweeping voltage is ranging from –0.6 to +0.8 V (versus Ag/AgCl). The redox currents and potentials are evaluated after removing the non-Faradaic current by background correction through the peak analysis in EC-Lab. CV is conducted by varying the scan rate from 50 – 300 mV/s (step size of 50 mV/s) to find out the nature of the electrochemical interface. CV at different concentrations of paracetamol ranging from 0.5 mM to 3 mM in steps of 0.5 mM is carried out to construct the calibration plots of the sensors.

3. Results

3.1. Morphological and structural characterization

The $ZnCr_xFe_{2-x}O_4$ ($x = 0$, 0.25, 0.5, 0.75, 1, 2) size and morphology are investigated by FESEM as shown in Fig. 1. Nanostructured particles with a similar morphology are observed in Fig. 1a–f. Particles aggregation is clear from the FESEM captures as previously reported in the literature [18,40–42]. This is due to the auto combustion synthesis method that does not allow for a strict control over the particle size or morphology. The particle size is estimated using ImageJ by taking a clear portion of the image with a low degree of aggregation, and the results are reported in Table 1. $ZnCr_xFe_{2-x}O_4$ ($x = 0.25$, 0.5, 0.75, 1, 2) showed similar particle size compared to the zinc ferrite ($x = 0$) that has slightly greater size (as it can be appreciated in Fig. 1f). It is possible that the particles are formed by more crystallites in the case of $x = 0$ compared to the other cases, as expected due to the synthesis method.

Fig. 2 depicts the surface of the $ZnCr_2O_4$ modified carbon working electrode at 1 μm scale (Fig. 2a) and 100 nm scale (Fig. 2b) respectively. The modified surface shows the very well dispersed nanoparticles of $ZnCr_2O_4$ (Fig. 2b) with a low degree of aggregation on the carbon surface.

To investigate the phase compositions of the samples and the crystallite dimensions, XRD analysis is conducted. The XRD patterns of $ZnCr_xFe_{2-x}O_4$ ($x = 0$, 0.25, 0.5, 0.75, 1, 2) are shown in Fig. 3.

For $x = 0$ and $x = 2$, the diffraction patterns fully match with those of the normal spinel Franklinite [43] ($ZnFe_2O_4$, ref. code 01–089–4926, ICSD-076,178) and Zincochromite [44] ($ZnCr_2O_4$, ref. code. 00–022–1107). Even for intermediate compositions, $ZnCr_xFe_{2-x}O_4$ spinel can be identified as the main crystalline phase, although the patterns are shifted in comparison to both Franklinite and Zincochromite. As a matter of fact, for x values between 0.25 and 1, these patterns exhibit a progressive shift of the spinel peaks toward lower angles as the Cr content increases. The intermediate position of the diffraction peaks between franklinite and zincochromite indicates that materials with intermediate composition may possess an intermediate structure between those of $ZnFe_2O_4$ and $ZnCr_2O_4$ an outcome similar to that of our previous study of $Zn_xNi_{1-x}Fe_2O_4$ nanomaterials [7]. This can be understood by taking a look into the cation distribution in the spinel oxides. Cations distribution can be affected by several factors such as ionic radii, electrostatic forces, crystal field stabilization energy and so forth [45]. Cr^{3+} ions generally form d^3 (high spin) complexes with a high octahedral crystal field stabilization energy (CFSE) of $-6/5\Delta_o$ (octahedral d-orbital splitting energy), eventually leading to a very high octahedral site preference energy (OSPE) as shown in Fig. 4. Fe^{3+} ions form d^5 high spin complexes (the weak ligand O^{2-} leads to lower Δ_o) with a zero CFSE and zero OSPE [46] (see Fig. 4) meaning that Fe^{3+} has no site preference; whereas Zn^{2+} has a very high tetrahedral site preference [7], which makes Fe^{3+} to occupy the octahedral sites. These facts suggest that $ZnCr_2O_4$ and $ZnFe_2O_4$ are normal spinels since mixing of Zn^{2+} with Cr^{3+} or Fe^{3+} in tetrahedral or octahedral sites is not possible. The progressive shift in the peaks because of the progressive change in the composition can be due to slight difference in ionic radii for Cr^{3+}(61.5pm) [47] and Fe^{3+}(64.5pm) [47] ions in the octahedral sites and/or due to stoichiometric mismatches occurring in the synthesized nanomaterials. Such a mismatch can produce stress/strain in the crystal structure which in turn leads planes to reflect at slightly modified 2θ angles [48].

Table 1
The average particle size of $ZnCr_xFe_{2-x}O_4$ nanomaterials.

Material	Particle size (nm)
$ZnFe_2O_4$	44 ± 17
$ZnCr_{0.25}Fe_{1.75}O_4$	29 ± 6
$ZnCr_{0.50}Fe_{1.50}O_4$	25 ± 5
$ZnCr_{0.75}Fe_{1.25}O_4$	26 ± 5
$ZnCrFeO_4$	26 ± 7
$ZnCr_2O_4$	20 ± 3

The XRD patterns of the intermediate compositions ($x = 0.25$, 0.5, 0.75, and 1) exhibit a small peak at a 2θ value equal to 26.5°, which corresponds to the position of the most intense peak of graphite. The presence of this crystalline phase is justifiable due to the synthesis process involving the use of a graphite reactor. However, it is not possible to identify the weakest peaks of graphite, likely due to the limited amount of this phase.

Finally, four small peaks can be observed in the XRD pattern of

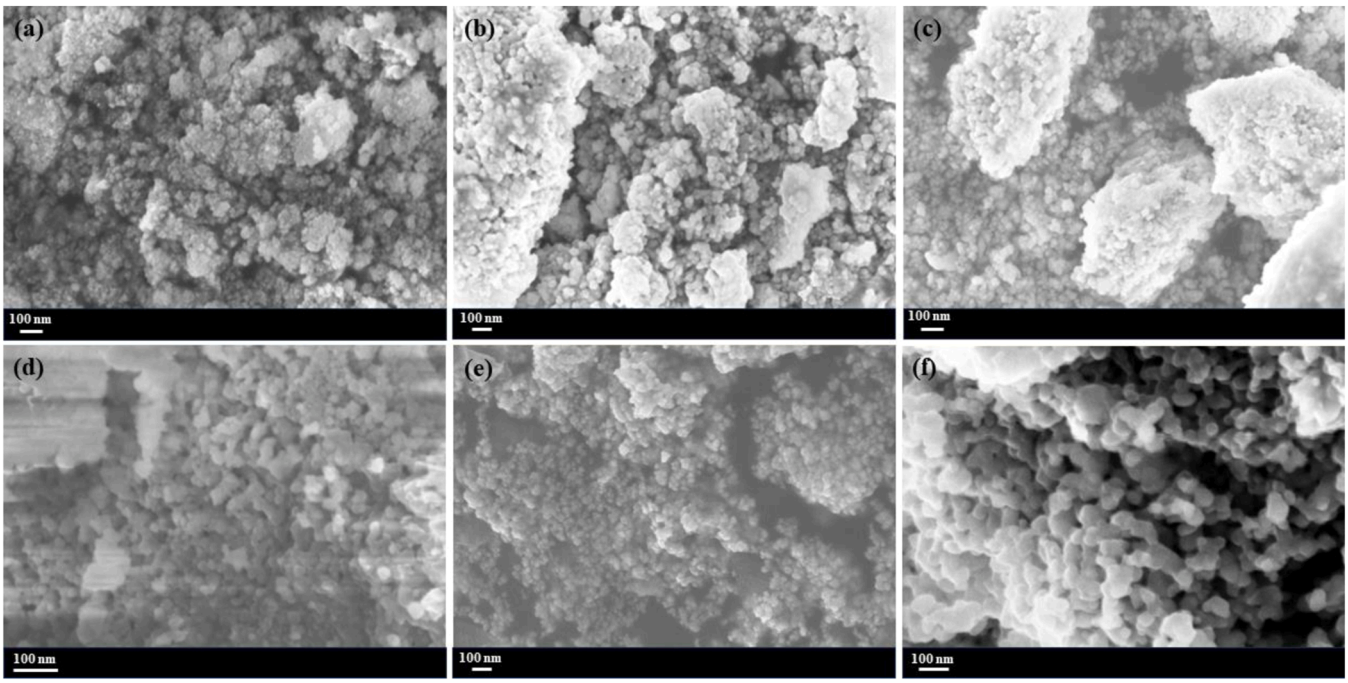

Fig. 1. FE-SEM images of (a) $ZnCr_2O_4$, (b) $ZnCrFeO_4$, (c) $ZnCr_{0.75}Fe_{1.25}O_4$, (d) $ZnCr_{0.5}Fe_{1.5}O_4$, (e) $ZnCr_{0.25}Fe_{1.75}O_4$, (f) $ZnFe_2O_4$.

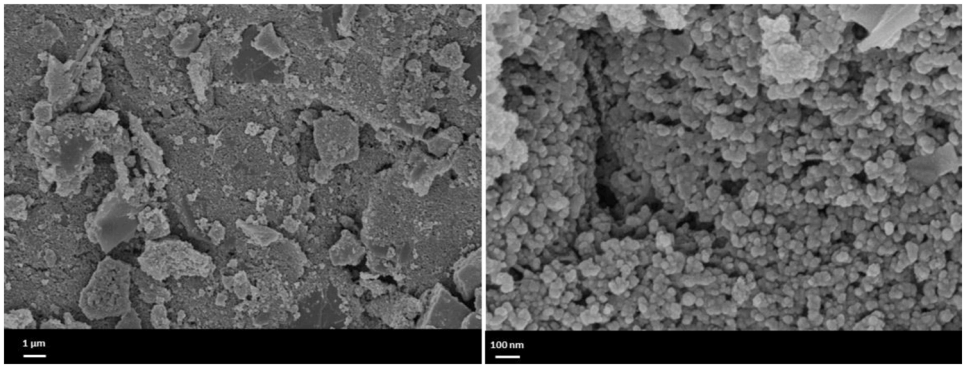

Fig. 2. FE-SEM image of $ZnCr_2O_4$ modified carbon working electrode surface (a) 5kx (1 µm) and (b) 50kx (100 nm) magnification, respectively.

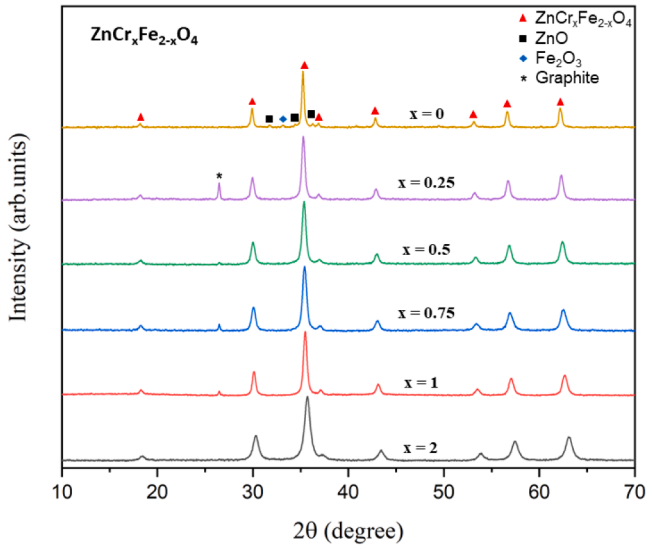

Fig. 3. XRD patterns of $ZnCr_xFe_{2-x}O_4$ nanomaterials showing different phases with surface oxides or defects.

$ZnFe_2O_4$ within the 2θ range between 30° and 36° These peaks are attributed to zinc oxide (ZnO, ref. code 01–080–0075, ICSD-067,849) and iron oxide (Fe_2O_3, ref. code 01–085–0987, ICSD-033,643) with their most intense peaks provided by the latter. Although the less intense peaks of these two phases could not be identified, their presence is clearly due to the reactants employed in the auto combustion synthesis. These extra phases of ZnO, Fe_2O_3 are mainly attributed to the surface states of the materials. Hence, they are difficult to detect by XRD if their presence is very low in proportion to the main spinel phase of the material.

The Debye-Scherrer's method is utilized to calculate the average crystallite size of the spinel oxides by taking the shape factor value as '0.9′ (assuming a spherical shape). Seven higher intensity peaks are considered corresponding to the diffraction of the (111), (220), (311), (400), (422), (511), and (440) planes, respectively. Microstrain is calculated using the same peaks. Table 2 shows the crystallite size and microstrain of each material. Crystallite size varies between 12 and 37 nm for $ZnCr_xFe_{2-x}O_4$ (x = 0, 0.25, 0.5, 0.75, 1, 2) materials. The calculated crystallite size from XRD and estimated particle size from FESEM are in good agreement with each other. Irregular variation of crystallite size is observed as the composition of the $ZnCr_2O_4$ changes by replacing Cr^{3+} with Fe^{3+}. These irregularities are quite common in the auto combustion synthesis because of the weak control over the crystallite growth kinetics leading to irregular variations in the nanoparticle size as witnessed by the FESEM analysis. Similar effects are shown in literature when combustion synthesis was used [7,8], for spinel oxides synthesis. Strain increased from $x = 2$ to $x = 1$ when the Cr:Fe is 1:1 and decreased

Table 2
The average crystallite size and microstrain of $ZnCr_xFe_{2-x}O_4$ nanomaterials.

Material	D (nm)	Strain (10^{-2})
$ZnFe_2O_4$	36.18 ± 1.38	0.3002 ± 0.0363
$ZnCr_{0.25}Fe_{1.75}O_4$	22.88 ± 1.15	0.3822 ± 0.0293
$ZnCr_{0.5}Fe_{1.5}O_4$	18.70 ± 0.62	0.3951 ± 0.0440
$ZnCr_{0.75}Fe_{1.25}O_4$	16.62 ± 0.69	0.4313 ± 0.0545
$ZnCrFeO_4$	20.10 ± 1.21	0.4357 ± 0.0621
$ZnCr_2O_4$	12.30 ± 0.16	0.3867 ± 0.0545

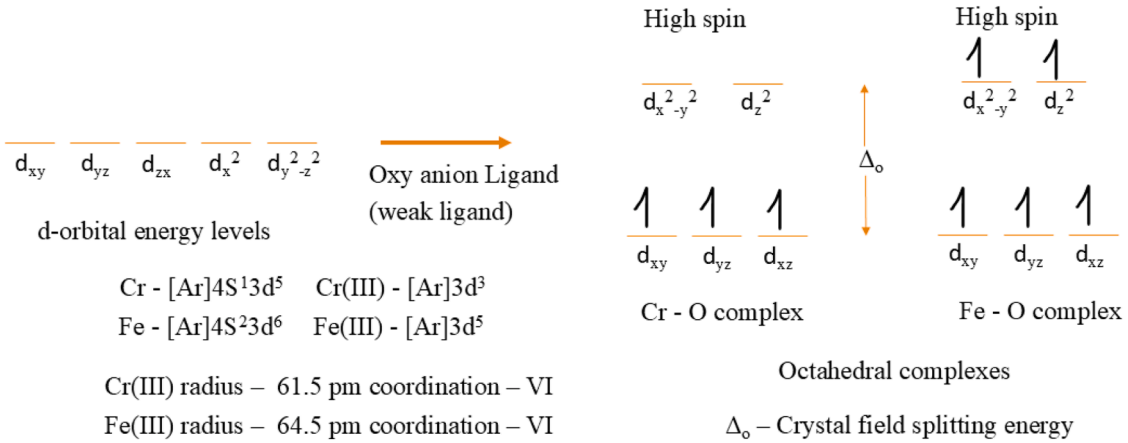

Fig. 4. Cr, Fe complexes with high spin crystal field stabilization energy.

when the content of Fe is higher than the content of Cr in the crystal structure (from $x = 0.75$ to 0.25). The strain further decreased when there is no Cr in the $ZnFeO_4$ structure meaning that a low ionic radius cation presence in the octahedral site has higher strain compared to the slightly higher ionic radius cation. These differences in strain justify the differences in 2θ angles for the planes of $ZnCr_xFe_{2-x}O_4$ ($x = 0$, 0.25, 0.5, 0.75, 1, 2) materials though they possess the same crystal structure.

The lattice constant 'a' of the nanomaterials is calculated using the typical relation of D-spacing and Miller indices of the planes. Five high intense planes (2 2 0), (3 1 1), (4 0 0), (5 1 1), and (4 4 0) are considered in calculating the lattice constant of each nanomaterial and the average lattice constant 'a' is reported in Table 3. The first thing to notice is that the lattice constant reported in the literature from the diffraction data of $ZnCr_2O_4$ is lower [44] than that of $ZnFe_2O_4$ [43], due to the higher ionic radius of Fe^{3+} compared to Cr^{3+}in the lattice structure following the Vegard's law [49]. The calculated lattice constants of $ZnCr_2O_4$ and $ZnFe_2O_4$ are in very good agreement with the reported lattice constants. From Table 3, the lattice constant decreases as the Cr content increases in the $ZnFe_2O_4$ lattice while for $x = 0.5$ and $x = 0.75$ the materials have a very similar 'a'. This behavior in the value of 'a' could be due to a minimal or negligible difference in local distortions in the lattice, resulting in a non-detectable change in 'a' value [48]. For $x = 0.25$ the 'a' value increased due to higher local distortion and further increased when Cr is completely replaced by Fe in the spinel.

The hopping length (L) (the average distance covered by an ion from one lattice site to another) is also determined using the equations reported in the literature [50]. The hopping length from 'Td' site (A-site) to 'Td' site (L_A), 'Oh' site (B-site) to 'Oh' site (L_B), and from A site to B-site ($L_{A\text{-}B}$) are listed in Table 4. The hopping lengths L_A and $L_{A\text{-}B}$ are greater than L_B leading to a lower probability of electron hopping. Hopping lengths can give an idea of the conductivity of the spinel nanomaterials as the motion of electrons decides the conductivity [27].

3.2. Spectroscopic characterization

Fig. 5a shows the Raman spectrum of $ZnCr_2O_4$. Previous studies indicate that $ZnCr_2O_4$ spinel has five Raman active modes [51]. The modes at 180, 510, and 589 cm^{-1} are due to $F_{2g}^{(3)}$, $F_{2g}^{(2)}$, and $F_{2g}^{(1)}$ symmetries of spinel, respectively. The high intense mode around 730 cm^{-1} corresponds to the Cr-O symmetric stretching vibration of $A_{1\ g}$ symmetry in CrO_6 octahedra. Another mode at 420 cm^{-1} is the E_g symmetry of spinel, while the peak at 340 cm^{-1} is due to the multiple phonon vibration of ZnO [52], this could be due to the surface ZnO of the spinel $ZnCr_2O_4$. The band around 820 cm^{-1} is assigned to O—Cr^{3+}-O symmetric stretching [53] because of the surface chromium hydroxide while the bands between 900 and 1000 cm^{-1} are assigned to Cr^{6+}-O due to the over oxidation of Cr [53] forming CrO_3 on the surface of the spinel. The Raman spectra of $ZnCr_xFe_{2-x}O_4$ ($x = 0$, 0.25, 0.5, 0.75, 1) nanomaterials are presented in Fig. 5b. As Fe is introduced in the $ZnCr_2O_4$ spinel, the bands between 900 and 1000 cm^{-1} disappear preventing the over oxidation of Cr. The bands around 820 cm^{-1} are still present due to the surface chromium hydroxide. The other bands of the spinel can be similarly assigned for the other Zn-Cr-Fe spinel nanomaterials. Pure zinc ferrite ($x = 0$) Raman spectrum interpretation is clearly presented in our previous work [7].

Table 3
Calculated lattice constant 'a' of $ZnCr_xFe_{2-x}O_4$ nanomaterials.

Material	'a' (Å)[C]	'a'(Å)[R]
$ZnFe_2O_4$	8.4465 ± 0.0069	8.443 [43]
$ZnCr_{0.25}Fe_{1.75}O_4$	8.4299 ± 0.0084	–
$ZnCr_{0.5}Fe_{1.5}O_4$	8.4178 ± 0.0076	–
$ZnCr_{0.75}Fe_{1.25}O_4$	8.4183 ± 0.0097	–
$ZnCrFeO_4$	8.3858 ± 0.0047	–
$ZnCr_2O_4$	8.3391 ± 0.0071	8.328 [44]

C – calculated from the experimental XRD data, R – reported in the literature diffraction data.

Table 4
Calculated hopping lengths of $ZnCr_xFe_{2-x}O_4$ nanomaterials.

Material	$L_{A\text{-}A}$ (Å)	$L_{B\text{-}B}$ (Å)	$L_{A\text{-}B}$ (Å)
$ZnFe_2O_4$	3.6575 ± 0.0030	2.9863 ± 0.0024	3.5018 ± 0.0029
$ZnCr_{0.25}Fe_{1.75}O_4$	3.6502 ± 0.0036	2.9804 ± 0.0029	3.4948 ± 0.0035
$ZnCr_{0.5}Fe_{1.5}O_4$	3.6449 ± 0.0033	2.9761 ± 0.0027	3.4898 ± 0.0032
$ZnCr_{0.75}Fe_{1.25}O_4$	3.6452 ± 0.0042	2.9763 ± 0.0034	3.4901 ± 0.0040
$ZnCrFeO_4$	3.6311 ± 0.0020	2.9648 ± 0.0017	3.4765 ± 0.0019
$ZnCr_2O_4$	3.6109 ± 0.0031	2.9483 ± 0.0025	3.4572 ± 0.0029

X-ray photoelectron spectroscopy (XPS) analysis is used to identify the chemical elements and oxidation states of elements present in the composition of spinel nanomaterials. Full XPS survey depicted in Fig. S1 showed no additional elements other than those expected in the spinels and adventitious carbon, excluding the presence of nitrates. High-resolution (HR) XPS spectra are acquired and analyzed (Fig. 6) to determine the oxidation states of Zn, Fe, Cr, and O in $ZnCr_xFe_{2-x}O_4$ nanomaterials. HR spectrum of O 1 s (Fig. 6d) is decomposed into three components, related to lattice oxygen O^{2-} (Zn-O, Fe-O, and Cr-O) at binding energy (BE) ≃ 529.9 eV, to hydroxyl groups (BE ≃ 531 eV), and to the adsorption of water (BE ≃ 533 eV) [7,54]. Fig. 6c shows the Zn 2p orbital splitting into Zn $2p_{1/2}$ and Zn $2p_{3/2}$ at 1044.1 eV and 1021.1 eV (ΔBE = 23 eV), respectively, attributed to tetrahedral Zn^{2+} in the spinel [7]. Fe 2p with Fe $2p_{1/2}$ and Fe $2p_{3/2}$ around 725.6 eV and 711.5 eV (ΔBE = 14.3 eV), respectively is complemented by the two shake-up satellites around 733.8 eV and 718.4 eV related to the presence of octahedral Fe^{3+} in spinel ferrites [7] (Fig. 6a). Cr $2p_{1/2}$ and Cr $2p_{3/2}$ peaks are decomposed using three components as shown in Fig. 6b. Photoelectron lines corresponding to 588 eV and 578.1 eV (ΔBE = 10.1 eV) are assigned to Cr^{3+} due to Cr bonding with hydroxyl groups (confirmed with O 1 s) forming Cr^{3+} hydroxide [55]. The components at 588 eV and 586.4 eV of Cr $2p_{1/2}$, 578.1 eV and 576.7 of Cr $2p_{3/2}$ are assigned to Cr^{3+} species present in the octahedral sites of the spinel and/or as Cr_2O_3 at the surface [51].

Diffuse Reflectance (DR) UV–Vis spectra of $ZnCr_xFe_{2-x}O_4$ nanomaterials are reported as Kubelka-Munk function [56] in Fig. 7. Zinc ferrite ($ZnFe_2O_4$) showed three main bands with maxima at ca. 300 nm, 500 nm and 800 nm (inset of Fig. 7). The most intense band with maximum at 300 nm can be ascribed to O^{2-}→ Fe^{3+} charge transfer transition (CT), usually giving rise to intense absorption [57]. The sample also absorbs in the visible range, with an absorption tail towards the Near Infra-Red (NIR) region. The band at 500 nm has been assigned in the literature to a CF transition $^6A_2 \rightarrow {}^4A_1$ (4E(4G)) of octahedral Fe^{3+}sites. This assignment is supported by the presence of the broad absorption centered at ca. 800 nm, assigned in literature to the $^6A_2 \rightarrow {}^4T_1$ (4G) transition of octahedral Fe^{3+} sites [7,58]. Accordingly, the bands at 500 nm and 800 nm are observed to decrease their intensity as Cr ions are introduced in the structure. Simultaneously, the band associated to O^{2-}→ Fe^{3+} CT transitions at 300 nm in the $ZnFe_2O_4$ sample decreased and a band at 275 nm is observed for $ZnCr_{0.75}Fe_{1.25}O_4$. The band at 275 nm is assigned to O^{2-}→ Cr^{3+} CT transitions in a matrix perturbed by the presence of Fe^{3+} ions. The bands at 255, 450 and 580 nm in the $ZnCr_2O_4$ sample, according to the literature, are due to O^{2-}→ Cr^{3+} CT transitions, $^4A_{2g} \rightarrow {}^4T_{1g}$(F) and $^4A_{2g} \rightarrow {}^4T_{2g}$ transition, respectively. The $ZnCr_2O_4$ sample also shows a minor band at 660 nm (inset of Fig. 7) that is assigned in the literature to $^4A_{2\ g} \rightarrow {}^4T_{1g}$(F) transition of octahedral Cr^{3+} (d^3) ions [59]. The same band occurs also in the samples containing both Cr and Fe, but slightly shifted and split, likely due to an effect of Fe in the matrix [60]. Another band at ca. 390 nm can be appreciated in the spectra of the $ZnCr_2O_4$ and cannot be assigned unambiguously, since it could be either due to the $^4A_{2\ g} \rightarrow {}^4T_{2\ g}$ transition of octahedral Cr^{3+} (d^3) ions [61] or to the O^{2-}→ Zn^{2+} CT transition.

The band gap energy (E_g) is calculated by using Tauc plot method by

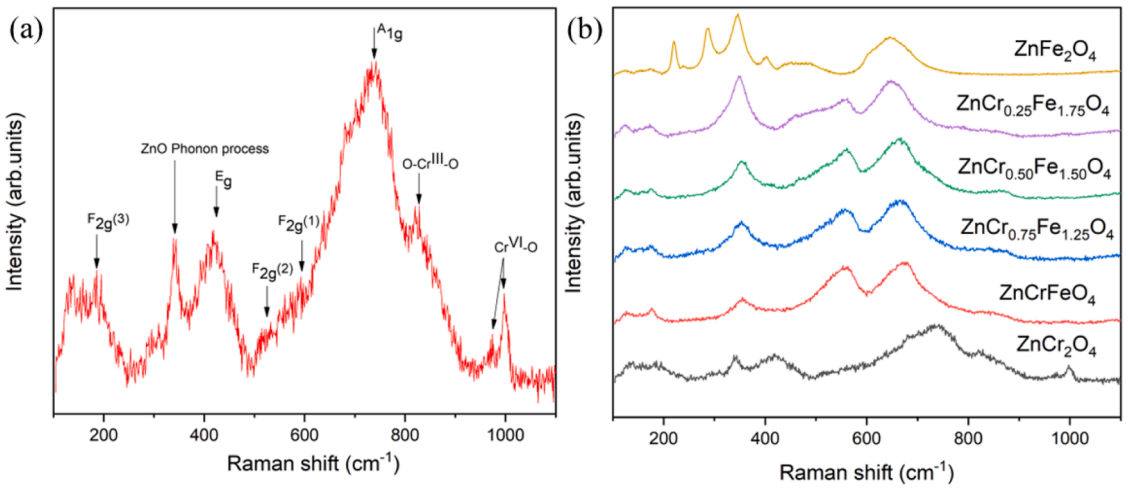

Fig. 5. Raman spectra of (a) of $ZnCr_2O_4$ nanomaterial and (b) $ZnCr_xFe_{2-x}O_4$ (x = 0, 0.25, 0.5, 0.75, 1, 2) nanomaterials.

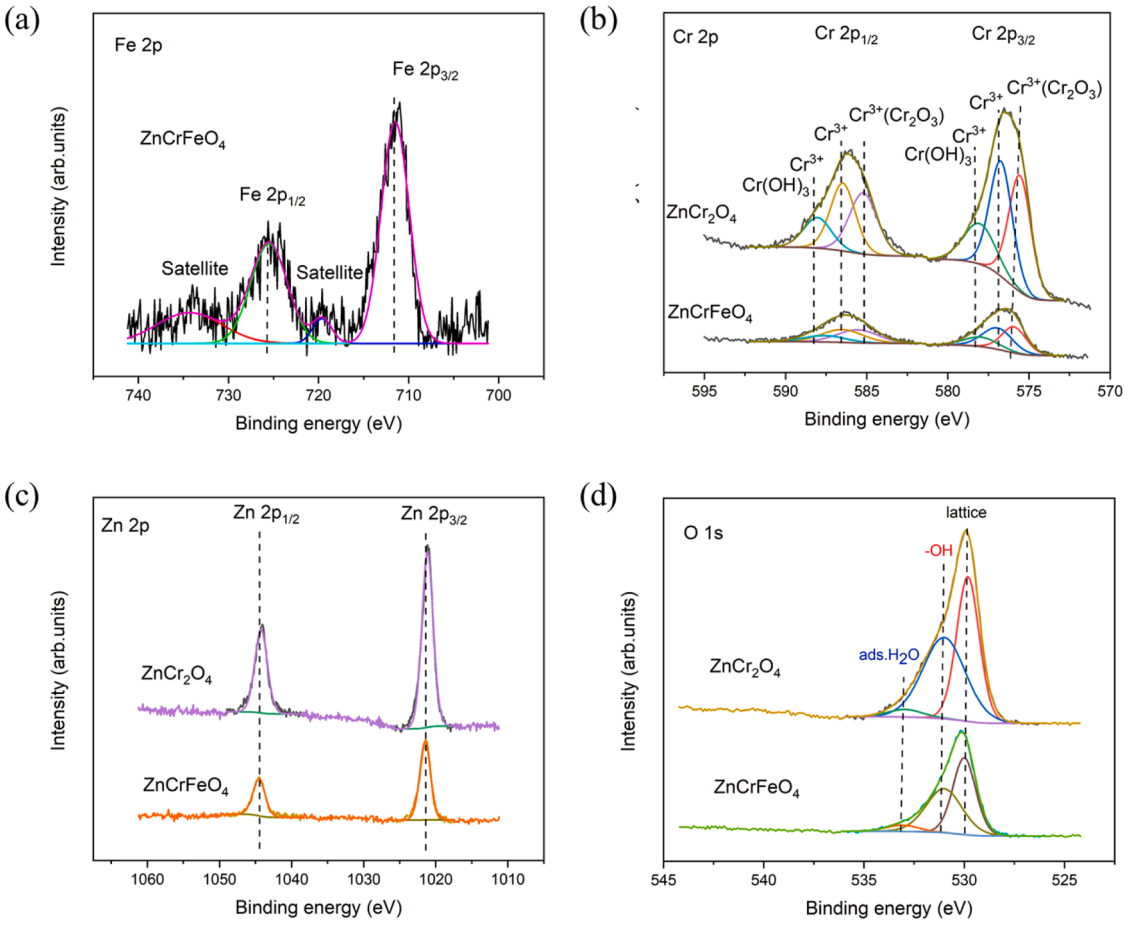

Fig. 6. High-resolution X-ray photoelectron spectra of the following lines: (a) Fe 2p, (b) Cr 2p, (c) Zn 2p, (d) O 1s.

assuming direct electron transition as in the earlier reported work [7]. The extrapolation of the Tauc plot is performed by considering the edges in such a way that the band tailing effect due to the presence of surface states (confirmed by XRD, Raman, and XPS) is included (Fig. S2, supporting information). The band gap is reported (Table 5) as an average band gap energy due to band tailing effect of surface oxides or hydroxides on the spinel $ZnCr_xFe_{2-x}O_4$ nanomaterials. The band gap decreased as the Cr ions are introduced into the $ZnFe_2O_4$ spinel, and decreased further as we increased the Cr ions content (x = 0.5). When we increase further the Cr ions in the spinel the band gap has increased and increased further when the Fe ions are completely replaced by Cr ions in the spinel. This can be due to the Moss-Brunstein effect when some states close to the conduction band edge (E_C) of a semiconductor are populated due to doping [61]. This is observed in both $ZnFe_2O_4$ and $ZnCr_2O_4$ spinel nanomaterials when Cr and Fe ions are introduced into the structure respectively, up to a certain concentration the band gap has decreased and higher concentration lead to an increase in E_g due to the CB edge being populated pushing the absorption edge to the higher

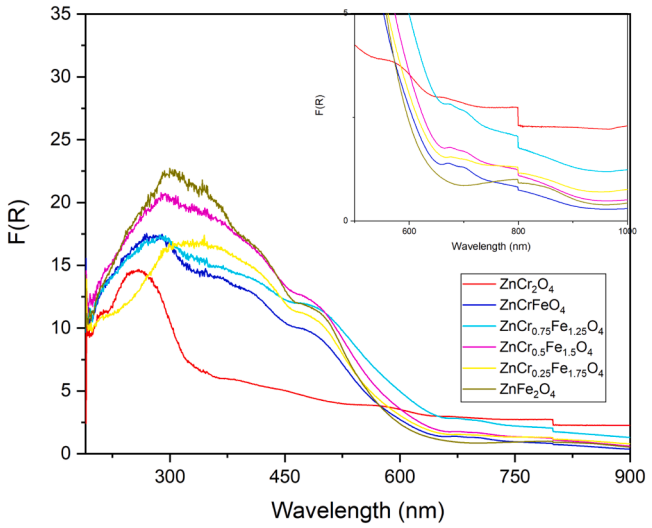

Fig. 7. DR UV–Vis spectra of $ZnCr_xFe_{2-x}O_4$ nanomaterials. The inset shows a magnification of the spectra in the 500–1000 nm range. The step at 800 nm is due to the change in the type of optical filter while the measurement was running.

Table 5
Estimated E_g, E_V, and E_C of $ZnCr_xFe_{2-x}O_4$ nanomaterials.

Material	Eg (eV)	Ev (eV)	Ec (eV)
$ZnFe_2O_4$	2.58 ± 0.06	−1.87 ± 0.49	0.71 ± 0.43
$ZnCr_{0.25}Fe_{1.75}O_4$	2.38 ± 0.06	−1.32 ± 0.43	1.06 ± 0.37
$ZnCr_{0.50}Fe_{1.50}O_4$	2.17 ± 0.01	−0.89 ± 0.27	1.28 ± 0.26
$ZnCr_{0.75}Fe_{1.25}O_4$	2.61 ± 0.12	−0.64 ± 0.21	1.97 ± 0.09
$ZnCrFeO_4$	2.78 ± 0.13	−0.94 ± 0.28	1.84 ± 0.15
$ZnCr_2O_4$	3.07 ± 0.11	−0.33 ± 0.09	2.74 ± 0.02

energy levels.

Valence band XPS spectra of $ZnCr_xFe_{2-x}O_4$ ($x = 0, 0.25, 0.5, 0.75, 1, 2$) nanomaterials are used to extract the energy of the valence band maximum (E_V) of each nanomaterial. The first rising edge of the valence band spectrum is extrapolated to the x-axis upon baseline correction and the x-intercept is taken as the energy level of the valence band maximum 'E_V' of the nanomaterial (Fig. S3, supporting information). The energy level of the conduction band minimum 'E_C' (=Eg+Ev) is calculated and the values E_g, E_V, and E_C reported in Table 5. The Fermi energy level (E_F) of nanomaterials is assumed to be at zero eV hence the E_V values are reported with a negative sign.

3.3. Electrochemical characterization

Initially bare, $ZnFe_2O_4$, and $ZnCr_2O_4$ sensors are characterized by electrochemical impedance spectroscopy with 4 mM ferri/ferrocyanide redox couple in 0.1 M PB at pH 7. Fig. S4 shows the Nyquist plots of the different sensor samples. The plots are fitted with equivalent Randels circuit, the series resistance (R_s) and the charge transfer resistance (R_{ct}) are reported in Table S1. Zinc ferrite and zinc chromite sensors have exhibited series resistances of 154 and 140 Ω while the charge transfer resistances are 2.7 and 3.7 kΩ, respectively, which are lower than the bare sensor (R_s = 168 Ω, R_{ct} = 5.8 kΩ) proving the effect of nanomaterials electrocatalytic activity in reducing the resistance at the electrochemical interface. Scan rate analysis is performed by cyclic voltammetry with scan rates from 25 mV/s to 150 mV/s in steps of 25 mV/s. Fig. S5 shows the CVs of bare, $ZnFe_2O_4$, and $ZnCr_2O_4$ sensors with respect to the scan rate and observed that the redox potential is increasing with an increase in scan rate. The inset shows that the oxidation current is varying linearly with the square root of the scan rate, by indicating that it is generated by a freely diffusing quasi-reversible electrochemical interface . Electroactive surface area (A_{R-S}; $A_{Real} = A_{R-S}/A_{geom}$; A_{geom} = 0.12 cm^2) of the three sensor' types are calculated using the Randles-Sevčik equation and reported in Table S2 [22,62]. The presence of nanostructured spinel nanomaterials increased the electroactive surface area compared to the bare carbon sensors as expected.

Fig. 8 shows the cyclic voltammograms of bare and $ZnCr_xFe_{2-x}O_4$ sensors for 1 mM paracetamol in 0.1 M PB at pH 7 at a scan rate of 100 mV/s. Preliminary observation is that $ZnCr_xFe_{2-x}O_4$ (x = 0, 0.25, 0.5, 0.75, 1, 2) sensors show enhanced performance compared to the bare carbon sensor. Higher current and lower overpotential are observed making the $ZnCr_xFe_{2-x}O_4$ sensors better than the bare carbon-based sensor. Among the $ZnCr_xFe_{2-x}O_4$ sensors, it is observed that pure $ZnFe_2O_4$ sensor resulted in higher oxidation current and lowest oxidation potential compared to the pure $ZnCr_2O_4$ sensor and mixed Cr-Fe sensors. Table 6 reports the oxidation current and potential (from here on all errors are reported as standard error mean (sem) unless otherwise specified) of bare and $ZnCr_xFe_{2-x}O_4$ sensors. Bare sensor has an oxidation potential of 396 ± 2 mV with an oxidation current of 34.5 ± 0.2 μA. $ZnCr_2O_4$ sensor produced a 13.21 μA higher current at a 104 mV lower overpotential compared to the bare one showing the impact of nanoparticles. When we replaced 50 % of Fe by Cr (x = 1) in the crystal lattice of $ZnFe_2O_4$, we observed a 7 mV lower oxidation potential, and a similar oxidation current compared to the pure chromite sensor. As the Cr % decreased (x = 0.75, 0.5, 0.25) in $ZnFe_2O_4$ structure, similar oxidation current and potential are noticed, indicating that lower amounts of Cr addition does not lead to a significant enhancement in the electrochemical performance. The pure ferrite sensor (x = 0) has produced a 152 mV lower potential and 17.9 μA higher oxidation current compared to the bare carbon one. The effect on the potential is clear evidence of the very well-known Nernst effect [7,62,63]. The presence of nanolayers at the interface between electrode and paracetamol shifts the redox reaction towards lower potential by using lower energy in electron transfer. The biggest advantage of using nanomaterials in electrochemical sensors is to use less energy to produce high oxidation currents for better detection of molecules.

3.3.1. Effect of scan rate

Cyclic voltammetry is carried out by varying the scan rate 'ν' from 50 mV/s to 300 mV/s (step size 50 mV/s). Fig. 9 shows the cyclic voltammograms of bare, $ZnCr_2O_4$, $ZnCrFeO_4$, and $ZnFe_2O_4$ sensors for 1 mM paracetamol in 0.1 M PB at pH 7. The inset of Fig. 9 shows the plots

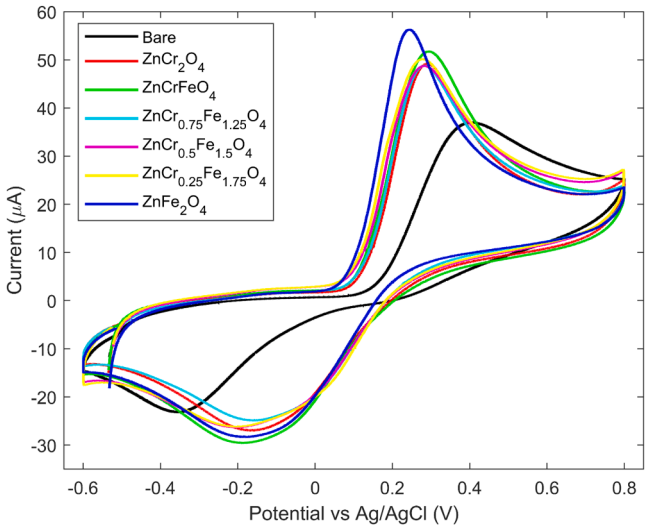

Fig. 8. Cyclic voltammograms of bare and $ZnCr_xFe_{2-x}O_4$ sensors with 1 mM paracetamol in 0.1 M PB at pH 7 (ν = 100 mV/s).

Table 6
Oxidation potential and current of the bare and $ZnCr_xFe_{2-x}O_4$ sensors.

Sensor	Oxidation potential (mV)	Oxidation Current (μA)
Bare	396 ± 2	34.50 ± 0.20
$ZnFe_2O_4$	244 ± 1	52.41 ± 0.56
$ZnCr_{0.25}Fe_{1.75}O_4$	280 ± 1	47.81 ± 0.26
$ZnCr_{0.50}Fe_{1.50}O_4$	285 ± 2	45.92 ± 0.12
$ZnCr_{0.75}Fe_{1.25}O_4$	282 ± 2	45.88 ± 0.39
$ZnCrFeO_4$	285 ± 2	47.68 ± 0.72
$ZnCr_2O_4$	292 ± 2	47.71 ± 1.20

of the redox currents with respect to $\sqrt{\nu}$. The oxidation current (I_{pa}) and reduction current (I_{pc}) vary linearly with $\sqrt{\nu}$ while the peak potential shifts to higher potentials as 'ν' increases. Linear regression equations of redox currents along with the regression coefficients for the bare and $ZnCr_xFe_{2-x}O_4$ (x = 0, 1, 2) sensors are reported in Table 7. The same effect is observed for $ZnCr_xFe_{2-x}O_4$ (x = 0.25, 0.5, 0.75) sensors, respective cyclic voltammograms at different scan rates are shown in Fig. **S6** (supporting information) and linear regression equations with regression coefficients are listed in Table **S3** (supporting information). The effect of 'ν' is explained using Randles-Sevčik theory [62,63],: as 'ν' increases the overall current increases due to the increase in capacitive current in addition to the faradaic current produced by the redox reaction at the interface. As the peak potential position changes with 'ν' and current varies linearly with $\sqrt{\nu}$ then the electrochemical system is a freely diffusing quasi-reversible electrochemical system.

Table 7
I_{pa}, I_{pc} regression equations of the bare and the $ZnCr_xFe_{2-x}O_4$ (x = 0, 1, 2) sensors.

Sensor	I_{pa}	R^2	I_{pc}	R^2
Bare	$2.82\sqrt{\nu}$ +6.35	0.998	$-2.26\sqrt{\nu}$ + 8.93	0.999
$ZnFe_2O_4$	$5.86\sqrt{\nu}$ +0.87	0.999	$-3.27\sqrt{\nu}$ + 4.35	0.991
$ZnCrFeO_4$	$5.96\sqrt{\nu}$ −8.9	0.999	$-3.71\sqrt{\nu}$ −7.21	0.997
$ZnCr_2O_4$	$4.91\sqrt{\nu}$ −1.7	0.999	$-3.32\sqrt{\nu}$ + 4.74	0.998

3.3.2. *Kinetic parameters*

Fig. 10 displays the potential values of the anodic (E_{pa}) and cathodic (E_{pc}) peak **potentials**, and peak-to-peak separation **potential** (ΔE_p) vs ln(ν) of the bare and $ZnCr_xFe_{2-x}O_4$ (x = 0, 1, 2) sensors. E_{pa}, E_{pc}, and ΔE_p are varying linearly with ln(ν) with linear regression parameters listed in Table 8, and Table 9. Similarly for the other sensors, peak potentials and ΔE_p with ln(ν) are depicted in Fig. **S7** and linear regression equations listed in Table **S4, S5** (supporting information), respectively. After checking the linearity of redox currents vs $\sqrt{\nu}$ and the linearity of E_{pa}, E_{pc}, and ΔE_p vs ln(ν), Laviron model [64] is applied to calculate the electron transfer rate coefficient (α), and kinetic rate constant (k). In Laviron model, E_{pc} and E_{pa} are given by

$$E_{pc} = E^0 - \left(\frac{RT}{\alpha nF}\right) ln\left[\frac{\alpha}{|m|}\right], \quad (1)$$

$$E_{pa} = E^0 + \left(\frac{RT}{(1-\alpha)nF}\right) ln\left[\frac{(1-\alpha)}{|m|}\right], \quad (2)$$

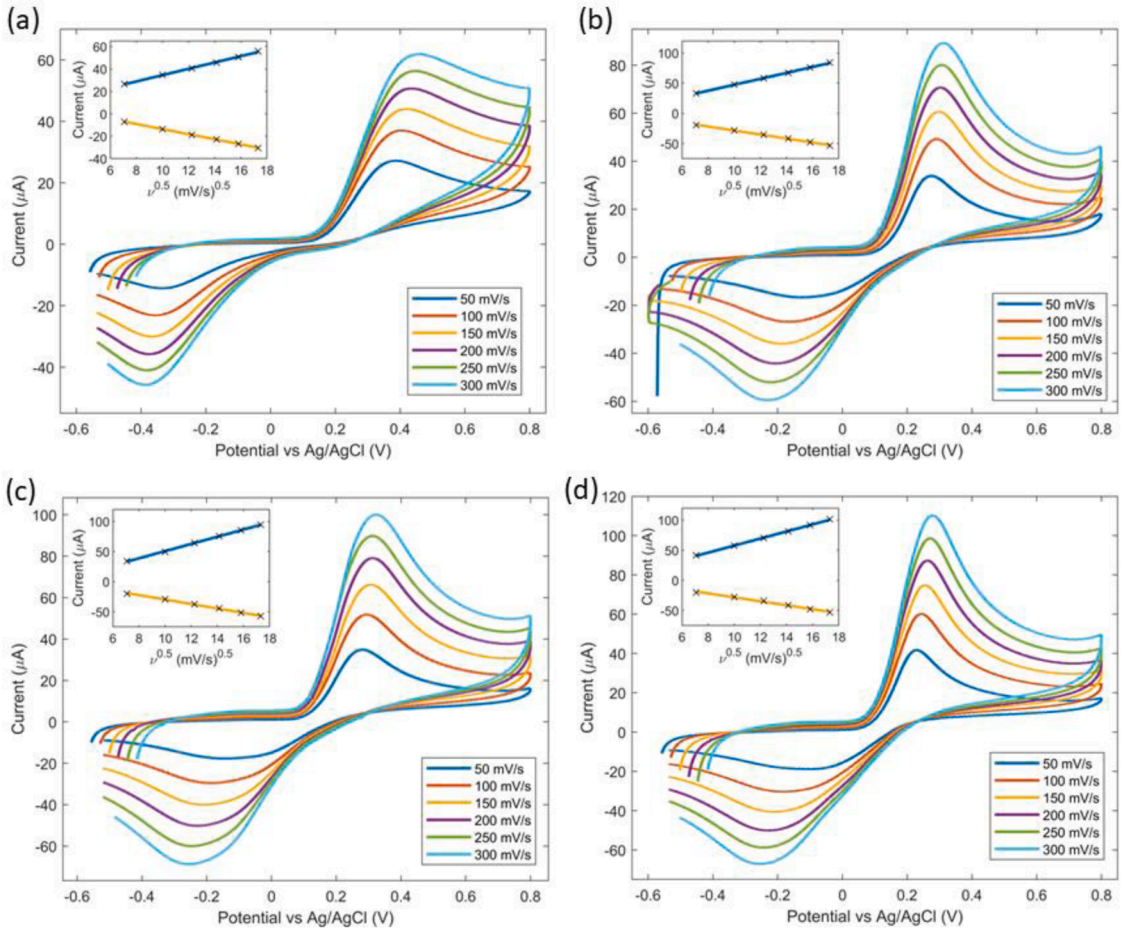

Fig. 9. Cyclic voltammograms of (a) bare (b) $ZnCr_2O_4$ (c) $ZnCrFeO_4$, and (d) $ZnFe_2O_4$ sensors with scan rate from 50 – 300 mV/s (step of 50 mV/s) with 1 mM paracetamol in 0.1 M PB at pH 7. Inset shows the redox current variation with $\sqrt{\nu}$.

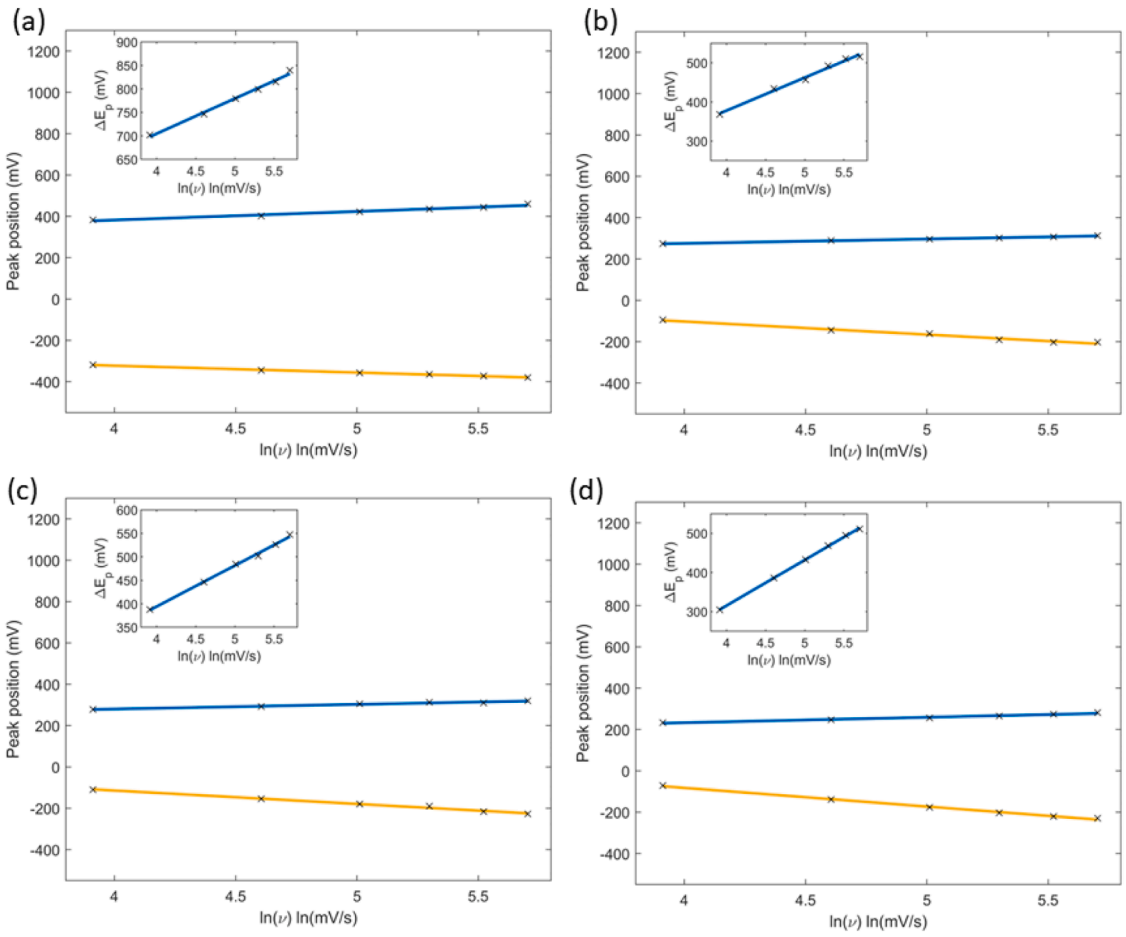

Fig. 10. Redox positions of (a) bare (b) $ZnCr_2O_4$ (c) $ZnCrFeO_4$, and (d) $ZnFe_2O_4$ sensors with ln(ν). Inset shows the ΔE_p variation with ln(ν).

Table 8
E_{pa}, E_{pc} regression equations for bare and $ZnCr_xFe_{2-x}O_4$ ($x = 0, 1, 2$) sensors.

Sensor	E_{pa}	R^2	E_{pc}	R^2
Bare	41.5 ln(ν) + 216.1	0.973	− 33.3 ln(ν) − 189.3	0.996
$ZnFe_2O_4$	26.4 ln(ν) + 127.3	0.975	− 90.2 ln(ν) − 278.3	0.996
$ZnCrFeO_4$	22.6 ln(ν) + 189.3	0.963	− 64.7 ln(ν) + 144.5	0.989
$ZnCr_2O_4$	21.1 ln(ν) + 190.8	0.995	− 63.2 ln(ν) + 150.4	0.981

Table 9
ΔE_p regression equations for bare and $ZnCr_xFe_{2-x}O_4$ ($x = 0, 1, 2$) sensors.

Sensor	ΔE_p	R^2
Bare	74.81 ln(ν) + 405.47	0.991
$ZnFe_2O_4$	116.64 ln(ν) − 151.01	0.999
$ZnCrFeO_4$	87.33 ln(ν) + 44.85	0.997
$ZnCr_2O_4$	84.3 ln(ν) + 40.4	0.989

where $m = (RT/F)(k/n\nu)$, 'n' is the number of electrons involved in the redox reaction, 'ν' is the scan rate, 'E^0' is the standard surface potential, 'R' is the universal gas constant, 'T' is the absolute temperature in Kelvin, and 'F' is the Faraday constant. 'α' value is evaluated from the slopes of the E_{pa} and E_{pc} versus ln(ν) plots. The kinetic rate constant 'k' is calculated using the Laviron equation for 'k':

$$\ln(k) = \alpha\ln(1-\alpha) + (1-\alpha)\ln(\alpha) - \ln\left(\frac{RT}{nF\nu}\right) - \alpha(1-\alpha)\frac{nF\Delta E_p}{RT} \quad (3)$$

Paracetamol redox process involves two electrons ($n = 2$) [7], and ΔE_p is chosen at $\nu = 100$ mV/s since the electrochemical system is a quasi-reversible system. The α, ΔE_p, and k values of the bare and $ZnCr_xFe_{2-x}O_4$ sensors are reported in Table 10. The electron transfer rate coefficient α, ΔE_p are reduced for $ZnCr_xFe_{2-x}O_4$ sensors compared to the bare sensor. As the ΔE_p is lower than the bare sensor, $ZnCr_xFe_{2-x}O_4$ sensors have the higher 'k' values leading to the faster electrochemical reactions at the sensor and paracetamol interface. The 'k' is usually referred to as the first-order kinetic rate constant as the Laviron model didn't consider the double layer and diffusion effects at the interface of interest. We **observe** from Table 10 that $ZnCr_2O_4$, $ZnCrFeO_4$, $ZnFe_2O_4$ sensors have 'k' values of 3.73 ± 0.55, 4.53 ± 0.54, 13.1 ± 2.8 ms^{-1}, respectively. As the Fe % increases in $ZnCr_2O_4$ from 0 to 50 %, the 'k' increased around 0.8 ms^{-1} then decreased and finally highly increased when Cr is completely replaced by Fe. Pure ferrite sensor is found to be the best in the aspect of kinetic performance among all the sensors studied in this work.

3.3.3. *Sensitivity and limit of detection*

Cyclic voltammograms are recorded at different concentrations of

Table 10
α, ΔEp, and k of the bare and $ZnCr_xFe_{2-x}O_4$ sensors.

Sensor	α	ΔEp (mV)	k (ms^{-1})
Bare	0.536 ± 0.004	746 ± 5	(2.22 ± 0.19) x 10^{-3}
$ZnFe_2O_4$	0.23 ± 0.02	386 ± 2	13.1 ± 2.8
$ZnCr_{0.25}Fe_{1.75}O_4$	0.32 ± 0.01	488 ± 4	0.88 ± 0.16
$ZnCr_{0.50}Fe_{1.50}O_4$	0.35 ± 0.01	455 ± 4	1.11 ± 0.06
$ZnCr_{0.75}Fe_{1.25}O_4$	0.355 ± 0.003	564 ± 7	0.18 ± 0.03
$ZnCrFeO_4$	0.24 ± 0.01	446 ± 2	4.53 ± 0.54
$ZnCr_2O_4$	0.258 ± 0.004	444 ± 6	3.73 ± 0.55

paracetamol at a fixed scan rate of 100 mV/s. Oxidation current is measured and averaged over three measurements at each concentration and calibration of each sensor is plotted. The calibration of each sensor is depicted in Fig. 11. The slope of the calibration of each sensor is the sensitivity of the sensor as listed in Table 11. Sensitivity has a two-fold increase (> 32 μA/mM) with respect to the bare sensor (16.7 ± 0.9 μA/mM) for $ZnCr_xFe_{2-x}O_4$ sensors. $ZnFe_2O$ sensor is the best (37.8 ± 0.2 μA/mM) while $ZnCrFeO_4$ tailored sensor is the second best. The limit of detection (LOD) is calculated using the relation LOD = KD/S, where K is the statistical confidence level, here it is set equal to '3', D is the standard deviation of the blank measurements, and 'S' is the sensitivity of the sensor. LOD for each sensor is reported in Table 11 where $ZnCrFeO_4$ sensor shows the lowest LOD of 1.94 ± 0.01 μM while $ZnFe_2O_4$ sensor has the highest LOD of 7.94 ± 0.04 μM among all the sensors in this work.

4. Discussion

This work used a simple, single-step, cost-effective, solvent-free, auto combustion synthesis to produce nano oxides. This synthesis has no control over the temperature of the reaction due to its exothermic (abrupt change in temperature due to the release of heat) nature. Despite this drawback the synthesis procedure is successful in producing the nanoparticles of interest. Another important factor is the shape of the particles which eventually impacts on the orientation leading to the different reactivity of the particles. This work has led to the successful production of uniform (almost) spherically shaped nanoparticles ruling out different orientation possibilities, even if a certain degree of aggregation is observed which can hinder the reactivity of some nanoparticles. This affects the performance of the working electrode participating in the electrochemical reaction leading to different reaction rates (different rate constant '*k*').

From XRD, it is proved that both $ZnFe_2O_4$ and $ZnCr_2O_4$ nanomaterials have a normal spinel structure; the conduction of spinel materials is explained by the 'small polaron hopping' model [7,27]. This model suggests that the conduction depends on the charge transfer between cations present in the 'Oh' sites of the spinel structure. Since both zinc ferrite and zinc chromite have a normal spinel, both Fe and Cr occupy the 'Oh' sites in the spinel, Fe and Cr share the 'Oh' sites in the case of other $ZnCr_xFe_{2-x}O_4$ (x = 0.25, 0.5, 0.75, 1) nanomaterials. In $ZnCr_2O_4$ and $ZnFe_2O_4$, conduction occurs due to electron hopping of Cr^{3+}/Cr^{4+} and Fe^{3+}/Fe^{2+}, respectively. According to hopping lengths of $ZnCr_xFe_{2-x}O_4$ (x = 0, 0.25, 0.5, 0.75, 1, 2) nanomaterials, the hopping

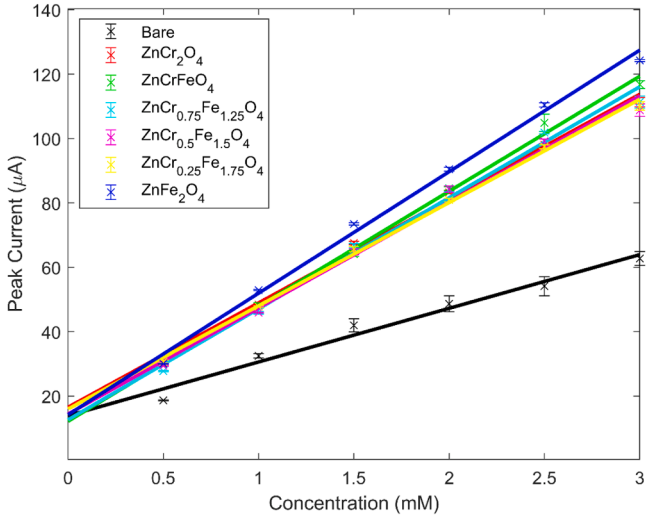

Fig. 11. Calibration of bare and $ZnCr_xFe_{2-x}O_4$ sensors for paracetamol (0.5 to 3 mM) in 0.1 M PB at pH 7.

Table 11
The sensitivity and limit of detection of the bare and $ZnCr_xFe_{2-x}O_4$ sensors.

Sensor	Sensitivity (μA/mM)	R^2	LOD (μM)
Bare	16.7 ± 0.9	0.975	3.26 ± 0.17
$ZnFe_2O_4$	37.8 ± 0.2	0.995	7.94 ± 0.04
$ZnCr_{0.25}Fe_{1.75}O_4$	32.1 ± 0.3	0.998	7.57 ± 0.08
$ZnCr_{0.50}Fe_{1.50}O_4$	33.3 ± 0.6	0.990	2.21 ± 0.04
$ZnCr_{0.75}Fe_{1.25}O_4$	34.5 ± 0.5	0.990	2.29 ± 0.03
$ZnCrFeO_4$	35.7 ± 0.1	0.996	1.94 ± 0.01
$ZnCr_2O_4$	32.4 ± 0.5	0.996	2.99 ± 0.05

length L_B (hopping length from B-site to B-site) decreases from $x = 0$ to 0.5 and $x = 0.75$ has a very similar L_B as $x = 0.5$ and then decreased for x = 1 and 2. The hopping length L_B suggests that the conductivity decreases as the hopping length increases [27] but the conductivity does not depend only on the hopping lengths of ions present in the spinel structure. The conductivity also depends on the hopping rate of electrons (jumps per second), a higher electron hopping rate results in a higher conductivity of the spinel nanomaterials [27]. The magnetic nature of the spinel structure (chromites typically exhibit an antiferromagnetic frustrated nature [65] and ferrites exhibit ferromagnetic behavior [26]) as well can affect the conductivity [27]. The sensitivity and rate constant increased from $x = 2$ to 1: this could be due to the equal proportion of Cr and Fe ions in the spinel leading to a higher conductivity compared to the pure chromite. When we moved from x = 1 to $x = 0.25$, the sensitivity and rate constant decreased, this might be due to the mismatches in the spinel system effecting the conductivity. The pure ferrite ($x = 0$) has the highest sensitivity and rate constant; this could well be due to the ferromagnetic nature of the ferrite with high conductivity compared to the other nanomaterials in the current study [27]. Table 12 shows the comparison of sensitivities and rate constants of different spinel oxides crystal structures from our previous work and the current work as well.

A normal spinel is a typical n-type semiconductor due to its conduction through electron hopping, whereas inverse spinel is a p-type one due to hole hopping conduction [27]. For this reason, a normal spinel conducts better compared to an inverse spinel. If we compare the current results with the previous work [7], the sensitivity and rate constant are higher compared to inverse spinel $NiFe_2O_4$, proving a better performance of normal spinel nanomaterials towards electrochemical sensing of paracetamol (Table 12). The mixed spinel with 'Zn' in nickel ferrite increased the sensitivity and rate constant compared to the pure inverse spinel nickel ferrite, whereas the presence of 'Bi' with mixed spinel has decreased the sensitivity. In the former the mixed effect is mainly due to bivalent cations of 'Zn' and 'Ni' whereas in the latter case the effect is due to the trivalent cations of 'Bi' and 'Fe'. This indicates that the mixed spinel based on the type of cations also plays an important role in the

Table 12
Comparison of electrochemical parameters for different spinel oxides with respect to their spinel structure.

Sensor	Sensitivity (μA/mM)	k (ms^{-1})	Spinel structure	Refs
$NiFe_2O_4$	29.4± **0.4**	0.27 ± 0.02	Inverse	[7]
$Zn_{0.4}Ni_{0.6}Fe_2O_4$	30.0 ± **0.2**	0.62 ± **0.10**	Mixed	[7]
$ZnFe_2O_4$	37.8 ± **0.2**	13.1 ± **2.8**	Normal	[7,22], **present work**
$ZnBiFeO_4$	25.6 ± **0.8**	1.3 ± **0.2**	Mixed	[22]
$ZnBi_2O_4$	23.5 ± 0.6	0.45 ± 0.16	Mixed	[22]
$ZnCrFeO_4$	35.7 ± **0.1**	4.5 ± 0.54	Normal	Present work
$ZnCr_2O_4$	32.4 ± **0.5**	3.73 ± **0.55**	Normal	Present work

electrochemical performance. Apart from the type of spinel, the ionic size also affects the electrochemical performance with a clear difference in sensitivity and rate constant with Bi(III) and Cr(III) in $ZnFe_2O_4$ (Table 12). We can predict the nature of the electron transfer by using the energy band gap of the nanomaterials. Similar to our previous work [7], Burello and Worth's theoretical predictive model [66,67] is employed to predict the electron transfer between the sensor surface and the molecule of interest. Energy band edges E_C and E_V of the nanomaterials are estimated using UV–vis spectroscopy and XPS techniques, and experimental redox potential (E_{pa}, E_{pc}) of paracetamol is used to predict the type of electron transfer. A matching of the E_C, E_V with E_{pa} and E_{pc} is depicted in Fig. 12. It is possible to estimate the electron transfer by considering the E_C of the nanomaterial and E_{pa} of paracetamol. A direct electron transfer is possible when the E_C is overlapping or below the E_{pa} of paracetamol meaning that the electrons from the HOMO (Highest Occupied Molecular Orbital) of paracetamol can jump or tunnel through the barrier directly to the conduction band of the nanomaterial. From Fig. 12 we can see only for $ZnFe_2O_4$, an overlap between its E_C and the E_{pa} of paracetamol indicating a direct electron transfer phenomenon between the sensing material and paracetamol. We can observe that E_C is moving towards the E_{pa} of paracetamol as the content of Cr^{3+} ions is decreased from $x = 2$ to 0.25 in $ZnFe_2O_4$, but in these cases it is difficult to predict the direct electron transfer because of no overlapping or higher energy level with E_{pa} of paracetamol. However, in these sensors, we observed the electron transfer and so did the redox mechanism of paracetamol at the electrochemical interface. Hence, it is difficult to estimate the electron transfer using this model since Burello and Worth's model disregards the role of surface states. In the case of $x = 0.25$ to 2, there could be an involvement of surface states or defects, the presence is confirmed by XRD, Raman, and XPS characterizations. The existence of energy states within the nanomaterial's band gap results in band tailing due to the influence of surface states/-defects. The energy states within the band gap can overlap with the E_{pa} of paracetamol providing a path to the electron from the HOMO of paracetamol to the nanomaterial. This type of electron transfer is referred to as surface-state-mediated electron transfer. This could be another reason why $ZnFe_2O_4$ sensor performs better at lesser E_{pa} compared to the other sensors leading to smaller ΔE_p and to faster reaction at the interface with a higher rate constant. Since the E_C of $x = 0.25$ to 2 nanomaterials are at higher energy levels compared to E_{pa} of paracetamol, the redox reactions happened at higher applied potentials compared to the $ZnFe_2O_4$ sensor. We can clearly observe this phenomenon from Table 6: $ZnCr_2O_4$ has the highest E_{pa} of 292 ± 2 mV while the $ZnCr_{0.25}Fe_{1.75}O_4$ sensor has an oxidation potential of 280 ± 1 mV.

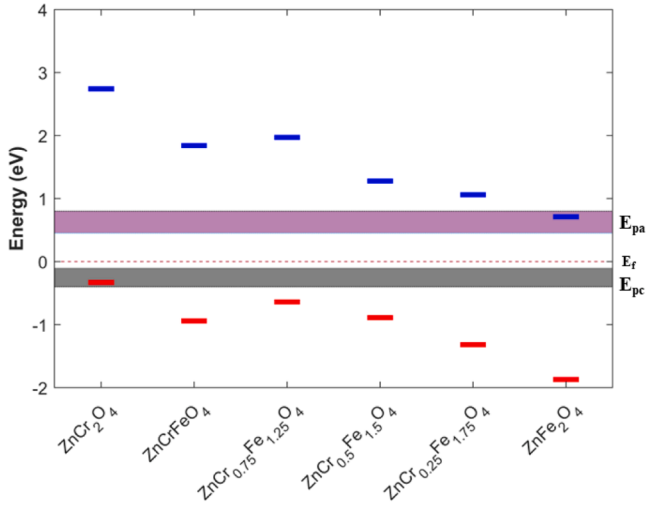

Fig. 12. Mapping of energy bands of $ZnCr_xFe_{2-x}O_4$ nanomaterials with redox potential (E_{pa} and E_{pc}) of paracetamol in predicting electron transfer mechanism at the electrochemical interface. E_f is the Fermi energy level of nanomaterials assumed to be at zero eV.

Another important factor to notice is that the ionic radius of Cr^{3+} is 61.5pm while that of Fe^{3+} is 64.5pm. A difference of 3pm (2.4 %) in ionic radius led to a change of 0.5 eV in the energy band gap. This difference in band gap has a relevant effect on the sensitivity and kinetic rate constant leading to different types of electron transfer mechanisms at the electrochemical interface. and how much the performance may be improved by a small alteration in the sensor surface. This further demonstrates how sensitive the electrochemical processes are at the electrochemical interface and a slight alteration in the sensor surface can enhance the performance significantly. Considering the possible valence states of Cr^{3+} compared to Fe^{3+}, there might be some possible intermediate reactions between chromites and paracetamol due to different reactivities of valence states of Cr^{3+} making the final reaction slower, hence leading to lower kinetic rate constant. This also justifies the higher kinetic rate constant for $ZnFe_2O_4$ sensor, and its higher sensitivity compared to all other sensors.

5. Conclusion

This work is a first-of-a-kind study of $ZnCr_xFe_{2-x}O_4$ ($x = 0$, 0.25, 0.5, 0.75, 1, 2) nanomaterials aimed to understand the effect of ionic radius and energy band gap on electrochemical sensing applications. A simple synthesis technique of auto combustion is used to synthesize the nanomaterials by using their respective metal nitrates in presence of urea as fuel and nanomaterials were extensively characterized. All spinel nanomaterials tailored sensors are found to have a sensitivity around two times higher than the bare sensors with a lower peak-to-peak potential and a higher kinetic rate constant. $ZnFe_2O_4$ is found to be the best material to maximize the sensitivity in electrochemical sensors, presenting the higher sensitivity and kinetic rate constant on the detection of paracetamol, used here as a model target. It was found that normal spinel nanomaterials work better in electrochemical sensing compared to inverse spinel. This is also due to the higher electrical conductivities related to the fact that conduction occurs by electron hopping in normal spinel while by hole hopping in inverse spinel. Energy band gap mapping with redox potential of paracetamol was performed to predict the electron transfer mechanism at the electrochemical interface. A slight change in the ionic radius produced a significant difference in the energy bandgap of nanomaterials. This proved how sensitive electrochemical reactions can be as a slight change at the interface can enhance the reaction efficiency significantly. The role of surface states in electrochemical electron transfer at the interface was thoroughly discussed.

We believe that the rational design of spinel-like nanomaterials can be used to design sensors for the realiable detection of different molecules, ranging from small molecules to dissolved oxygen, pH, and any other drugs/biomolecules of interest in biomedical applications.

CRediT authorship contribution statement

Mallikarjun Madagalam: Writing – original draft, Methodology, Investigation, Formal analysis, Data curation, Conceptualization. **Mattia Bartoli:** Writing – review & editing, Validation, Supervision, Conceptualization. **Michele Rosito:** Resources, Formal analysis. **Nicola Blangetti:** Resources, Formal analysis. **Marco Etzi:** Resources, Formal analysis, Data curation. **Elisa Padovano:** Validation, Resources. **Barbara Bonelli:** Writing – review & editing, Validation, Resources. **Sandro Carrara:** Writing – review & editing, Validation, Supervision. **Alberto Tagliaferro:** Writing – review & editing, Supervision, Resources.

Declaration of competing interest

The authors declare that they have no known competing financial

interests or personal relationships that could have appeared to influence the work reported in this paper.

Funding sources

No external funding is received.

Data availability statement

The data supporting this study's findings are available from the corresponding author upon reasonable request.

Supplementary materials

Supporting information provides the XPS survey spectra, Tauc plots, XPS Valence band spectra, cyclic voltammograms with scan rate, and redox potentials and peak-to-peak separation with ln(ν) of selected sensors.

Supplementary material associated with this article can be found, in the online version, at doi:10.1016/j.materresbull.2024.113191.

Data availability

Data will be made available on request.

References

[1] S.J. Yoon, S.H. Lee, K.H. Kim, K.S. Ahn, Electrical and magnetic properties of spinel $ZnCr_{2-x}Fe_xO_4$ ($0 \leq x \leq 1.0$), Mater. Chem. Phys. 73 (2) (2002) 330–334.
[2] N. Ponpandian, P. Balaya, A. Narayanasamy, Electrical conductivity and dielectric behaviour of nanocrystalline $NiFe_2O_4$ Spinel, J. Phys. Condens. Matter 14 (2002) 3221.
[3] D.R. Patil, B.K. Chougule, Effect of copper substitution on electrical and magnetic properties of $NiFe_2O_4$ Ferrite, Mater. Chem. Phys. 117 (1) (2009) 35–40.
[4] J.M. Gonçalves, L.V.de Faria, A.B. Nascimento, R.L. Germscheidt, S. Patra, L. P. Hernández-Saravia, J.A. Bonacin, R.A.A. Munoz, L. Angnes, Sensing performances of spinel Ferrites MFe_2O_4 (M = Mg, Ni, Co, Mn, Cu and Zn) based electrochemical sensors: a review, Anal. Chim. Acta 1233 (2022) 340362.
[5] P. Guo, L. Cui, Y. Wang, M. Lv, B. Wang, X.S. Zhao, Facile synthesis of $ZnFe_2O_4$ nanoparticles with tunable magnetic and sensing properties, Langmuir 29 (28) (2013) 8997–9003.
[6] P. Maji, R.B. Choudhary, Facile synthesis, dielectric properties and electrocatalytic activities of PMMA-$NiFe_2O_4$ nanocomposite, Mater. Chem. Phys. 193 (2017) 391–400.
[7] M. Madagalam, M. Bartoli, M. Rosito, N. Blangetti, M. Etzi Coller Pascuzzi, E. Padovano, B. Bonelli, S. Carrara, A. Tagliaferro, Unraveling the effect of the chemical and structural composition of $Zn_xNi_{1-x}Fe_2O_4$ on the electron transfer at the electrochemical interface, Small Struct. 4 (12) (2023) 2300163.
[8] Y. Köseoğlu, A. Baykal, F. Gözüak, H. Kavas, Structural and magnetic properties of $Co_xZn_{1-x}Fe_2O_4$ nanocrystals synthesized by microwave method, Polyhedron 28 (14) (2009) 2887–2892.
[9] A. Kumar, P. Sharma, D. Varshney, Structural, vibrational and dielectric study of Ni doped spinel Co ferrites: $Co_{1-x}Ni_xFe_2O_4$ (X=0.0, 0.5, 1.0), Ceram. Int. 40 (8, Part B) (2014) 12855–12860.
[10] F. Goga, R.A. Bortnic, A. Avram, M. Zagrai, L. Barbu Tudoran, R.A. Mereu, The effect of Ni^{2+} ions substitution on structural, morphological, and optical properties in $CoCr_2O_4$ matrix as pigments in ceramic glazes, Materials 15 (24) (2022), https://doi.org/10.3390/ma15248713.
[11] A.C.F.M. Costa, E. Tortella, M.R. Morelli, M. Kaufman, R.H.G.A. Kiminami, Effect of heating conditions during combustion synthesis on the characteristics of $Ni_{0.5}Zn_{0.5}Fe_2O_4$ nanopowders, J. Mater. Sci. 37 (17) (2002) 3569–3572, https://doi.org/10.1023/A:1016528302082.
[12] S. Sanjabi, A. Obeydavi, Synthesis and characterization of nanocrystalline $MgAl_2O_4$ spinel via modified Sol–Gel method, J. Alloys. Compd. 645 (2015) 535–540.
[13] F. Moradnia, S. Taghavi Fardood, A. Ramazani, S. Osali, I. Abdolmaleki, Green sol–gel synthesis of $CoMnCrO_4$ spinel nanoparticles and their photocatalytic application, Micro Nano Lett. 15 (10) (2020) 674–677.
[14] P. Sivakumar, R. Ramesh, A. Ramanand, S. Ponnusamy, C. Muthamizhchelvan, Synthesis and characterization of $NiFe_2O_4$ nanoparticles and nanorods, J. Alloy Compd. 563 (2013) 6–11.
[15] K.N. Nithyayini, M.N.K. Harish, K.L. Nagashree, Electrochemical detection of nitrite at $NiFe_2O_4$ nanoparticles synthesised by solvent deficient method, Electrochim. Acta 317 (2019) 701–710.
[16] R. Liu, M. Lv, Q. Wang, H. Li, P. Guo, X.S. Zhao, Solvothermal synthesis of size-tunable $ZnFe_2O_4$ colloidal nanocrystal assemblies and their electrocatalytic activity towards Hydrogen Peroxide, J. Magn. Magn. Mater. 424 (2017) 155–160.
[17] A. Sasmal, A.K. Nayak, Morphology-dependent solvothermal synthesis of spinel $NiCo_2O_4$ nanostructures for enhanced energy storage device application, J. Energy Storage 58 (2023) 106342.
[18] M.A.S. Amulya, H.P. Nagaswarupa, M.R.A. Kumar, C.R. Ravikumar, S. C. Prashantha, K.B. Kusuma, Sonochemical synthesis of $NiFe_2O_4$ nanoparticles: characterization and their photocatalytic and electrochemical applications, Appl. Surf. Sci. Adv. 1 (2020) 100023.
[19] D. Ghanbari, M. Salavati-Niasari, M. Ghasemi-Kooch, A sonochemical method for synthesis of Fe_3O_4 nanoparticles and thermal stable PVA-based magnetic nanocomposite, J. Ind. Eng. Chem. 20 (6) (2014) 3970–3974.
[20] S. Larumbe, J.I. Pérez-Landazábal, J.M. Pastor, C. Gómez-Polo, Sol-Gel $NiFe_2O_4$ nanoparticles: effect of the silica coating, J. Appl. Phys. 111 (10) (2012) 103911.
[21] P. Ma, Q. Geng, X. Gao, S. Yang, G. Liu, $CuCr_2O_4$ spinel ceramic pigments synthesized by sol-gel self-combustion method for solar absorber coatings, J. Mater. Eng. Perform. 25 (7) (2016) 2814–2823.
[22] M. Madagalam, M. Rosito, N. Blangetti, M. Etzi, E. Padovano, B. Bonelli, S. Carrara, A. Tagliaferro, M. Bartoli, Unveiling the effect of Bi in $ZnFe_2O_4$ nanoparticles in electrochemical sensors, Appl. Surf. Sci. 2024 (2024) 160870.
[23] S. Rajadurai, Synthesis, structural characterization and catalytic study of $ZnCrFeO_4$ spinel, Mater. Chem. Phys. 16 (5) (1987) 459–466.
[24] M.A. Kassem, A. Abu El-Fadl, A.M. Nashaat, H. Nakamura, Structure, optical and varying magnetic properties of insulating MCr_2O_4 (M= Co, Zn, Mg and Cd) nanospinels, J. Alloys. Compd. 790 (2019) 853–862.
[25] H. Tajizadegan, A. Heidary, O. Torabi, M.-H. Golabgir, A. Jamshidi, Synthesis and characterization of $ZnCr_2O_4$ nanospinel prepared via homogeneous precipitation using urea hydrolysis, Int. J. Appl. Ceram. Technol. 13 (2) (2016) 289–294.
[26] S. Ayyappan, S.P. Raja, C. Venkateswaran, J. Philip, B. Raj, Room temperature ferromagnetism in vacuum annealed $ZnFe_2O_4$ nanoparticles, Appl. Phys. Lett. 96 (14) (2010) 143106.
[27] O.M. Hemeda, M.M. Barakat, Effect of hopping rate and jump length of hopping electrons on the conductivity and dielectric properties of Co–Cd ferrite, J. Magn. Magn. Mater. 223 (2) (2001) 127–132.
[28] Y. Huang, Y. Tang, S. Xu, M. Feng, Y. Yu, W. Yang, H. Li, A highly sensitive sensor based on ordered mesoporous $ZnFe_2O_4$ for electrochemical detection of dopamine, Anal. Chim. Acta 1096 (2020) 26–33.
[29] L. Ning, X. Guan, J. Ma, M. Wang, X. Fan, G. Zhang, F. Zhang, W. Peng, Y. Li, A highly sensitive nonenzymatic H_2O_2 sensor based on platinum, $ZnFe_2O_4$ functionalized reduced graphene oxide, J. Alloys. Compd. 738 (2018) 317–322.
[30] C. Fan, L. Chen, R. Jiang, J. Ye, H. Li, Y. Shi, Y. Luo, G. Wang, J. Hou, X. Guo, $ZnFe_2O_4$ nanoparticles for electrochemical determination of trace Hg(II), Pb(II), Cu (II), and glucose, ACS Appl. Nano Mater. 4 (4) (2021) 4026–4036.
[31] Z. Shahnavaz, F. Lorestani, Y. Alias, P.M. Woi, Polypyrrole–$ZnFe_2O_4$ magnetic nano-composite with core–shell structure for glucose sensing, Appl. Surf. Sci. 317 (2014) 622–629.
[32] M. Madagalam, M. Bartoli, S. Carrara, A. Tagliaferro, ZnMxFe2-xO4 (M=Cr, Bi) Nanoparticles-Modified Electrochemical Sensors: Effect on Sensitivity and First-Order Kinetic Rate Constant. IEEE BioSensors Conference (BioSensors), London, United Kingdom, 2023, pp. 1–4, https://doi.org/10.1109/BioSensors58001.2023.10280910.
[33] M. Madagalam, M. Bartoli, S. Carrara, A. Tagliaferro, $ZnCr_{2-x}Fe_xO_4$ Nanoparticles-Modified Electrochemical Sensors: A Comparative Study, in: IEEE SENSORS, 2023, pp. 01–04.
[34] J.N. Baby, B. Sriram, S.-F. Wang, M. George, Versatile deep eutectic solvent assisted synthesis of ZnB_2O_4 (B = Al, Co, Cr) spinels: the effect of B site variants for comparing the bifunctional electrochemical sensing application, Chem. Eng. J. 435 (2022) 134136.
[35] Y. Fujio, V.V. Plashnitsa, M. Breedon, N. Miura, Construction of sensitive and selective zirconia-based CO sensors using $ZnCr_2O_4$-based sensing electrodes, Langmuir 28 (2) (2012) 1638–1645.
[36] B. Sriram, S. Kogularasu, S.-F. Wang, J.-K. Sheu, Deep eutectic solvent-mediated synthesis of spinel zinc chromite nanoparticles: a simple label-free electrochemical sensor for dopamine and ascorbic acid, ACS Appl. Nano Mater. (2023), https://doi.org/10.1021/acsanm.3c02775.
[37] R.A. Marcus, On the theory of oxidation-reduction reactions involving electron transfer. I, J. Chem. Phys. 24 (5) (1956) 966–978.
[38] R.A. Marcus, On the theory of oxidation-reduction reactions involving electron transfer. II. Applications to data on the rates of isotopic exchange reactions, J. Chem. Phys. 26 (4) (1957) 867–871.
[39] M. Tachiya, Generalization of the Marcus equation for the electron-transfer rate, J. Phys. Chem. 97 (22) (1993) 5911–5916.
[40] A. Hamed, A.G. Fitzgerald, L. Wang, M. Gueorguieva, R. Malik, A. Melzer, Synthesis, characterization and surface modification of $ZnCrFeO_4$ nanoparticles, Mater. Sci. Eng. C 33 (3) (2013) 1623–1628.
[41] Z. Mousavi, F. Soofivand, M. Esmaeili-Zare, M. Salavati-Niasari, S. Bagheri, $ZnCr_2O_4$ nanoparticles: facile synthesis, characterization and photocatalytic Properties, Sci. Rep. 6 (1) (2016) 20071.
[42] R.P. Patil, S.D. Delekar, D.R. Mane, P.P. Hankare, Synthesis, structural and magnetic properties of different metal ion substituted nanocrystalline zinc ferrite, Results Phys. 3 (2013) 129–133.
[43] J.M. Hastings, L.M. Corliss, Neutron diffraction studies of zinc ferrite and nickel ferrite, Rev. Mod. Phys. 25 (1) (1953) 114–119.
[44] H.F. McMurdie, M.C. Morris, J. deGroot, Crystallography of some double sulfates and chromates, J. Res. Natl. Bur. Stand. A. Phys. Chem. 75A (5) (1971).
[45] K. Kugimiya, H. Steinfink, Influence of crystal radii and electronegativities on the crystallization of AB_2X_4 stoichiometries, Inorg. Chem. 7 (9) (1968) 1762–1770.

[46] C. Suchomski, C. Reitz, K. Brezesinski, C. Tavares de Sousa, M. Rohnke, K. Iimura, Esteves de Araujo, T. Brezesinski, Structural, optical, and magnetic properties of highly ordered mesoporous MCr_2O_4 and $MCr_{2-x}Fe_xO_4$ (M = Co, Zn) spinel thin films with uniform 15 Nm diameter pores and tunable nanocrystalline domain sizes, Chem. Mater. 24 (1) (2012) 155–165.
[47] L.H. Ahrens, The use of ionization potentials part 1. Ionic radii of the elements, Geochim. Cosmochim. Acta 2 (3) (1952) 155–169.
[48] N. Hasan, S.S. Nishat, S. Sadman, M.R. Shaown, M.A. Hoque, M. Arifuzzaman, A. Kabir, Magnetic, optoelectronic, and rietveld refined structural properties of Al^{3+} substituted nanocrystalline Ni-Cu spinel ferrites: an experimental and DFT based study, J. Magn. Magn. Mater. 573 (2023) 170675.
[49] K.R. Rahman, F.-U.-Z. Chowdhury, M.N.I. Khan, Influence of Al^{3+} substitution on the electrical resistivity and dielectric behavior of $Ni_{0.25}Cu_{0.20}Zn_{0.55}Al_xFe2\text{-}_xO4$ ferrites synthesized by solid state reaction technique, J. Magnet. Magnet. Mater. 443 (2017) 366–373.
[50] E.H. El-Ghazzawy, M.A. Amer, Structural, elastic and magnetic studies of the as-synthesized $Co1-_xSr_xFe_2O_4$ nanoparticles, J. Alloys. Compd. 690 (2017) 293–303.
[51] W. Huang, W. Zha, D. Zhao, S. Feng, The effect of active oxygen species in nano-$ZnCr_2O_4$ spinel oxides for methane catalytic combustion, Solid State Sci. 87 (2019) 49–52.
[52] J. Xu, W. Ji, X.B. Wang, H. Shu, Z.X. Shen, S.H. Tang, Temperature dependence of the Raman scattering spectra of Zn/ZnO nanoparticles, J. Raman Spectrosc. 29 (7) (1998) 613–615.
[53] Yang, J. (Jeanne), Martens, W.N., Frost, R.L., Transition of chromium oxyhydroxide nanomaterials to chromium oxide: a hot-stage Raman spectroscopic study. *J. Raman Spectrosc.* 42 (5) (2011) 1142–1146.
[54] M. Etzi Coller Pascuzzi, A.J.W. Man, A. Goryachev, J.P. Hofmann, E.J.M. Hensen, Investigation of the stability of NiFe-(oxy)hydroxide anodes in alkaline water electrolysis under industrially relevant conditions, Catal. Sci. Technol. 10 (16) (2020) 5593–5601.
[55] M.C. Biesinger, B.P. Payne, A.P. Grosvenor, L.W.M. Lau, A.R. Gerson, R.S.C. Smart, Resolving surface chemical states in XPS analysis of first row transition metals, oxides and hydroxides: Cr, Mn, Fe, Co and Ni, Appl. Surf. Sci. 257 (7) (2011) 2717–2730.
[56] K. Dahm, D. Dahm, Principles of diffuse reflectance spectroscopy. Handbook Near-Infrared Analysis, 2021.
[57] X. Xu, A.K. Azad, J.T.S. Irvine, Photocatalytic H_2 generation from spinels $ZnFe_2O_4$, $ZnFeGaO_4$ and $ZnGa_2O_4$, Catal. Today 199 (2013) 22–26.
[58] K.W. Blazey, Wavelength-modulated Spectra of Some Fe^{3+} oxides, J. Appl. Phys. 45 (5) (2003) 2273–2280.
[59] D. Gingasu, I. Mindru, L. Patron, D.C. Culita, J.M. Calderon-Moreno, L. Diamandescu, M. Feder, O. Oprea, Precursor method—a nonconventional route for the synthesis of $ZnCr_2O_4$ spinel, J. Phys. Chem. Solids 74 (9) (2013) 1295–1302.
[60] A. Basak, L. Ramrakhiani, S. Ghosh, R. Sen, A.K. Mandal, Preparation of chromium doped phosphate glass adopting microwave irradiation and comparative analysis of properties with conventional glass, J. Non-Crystal. Solids 500 (2018) 11–17.
[61] L. Gomathi Devi, B. Narasimha Murthy, Characterization of Mo doped TiO_2 and its enhanced photo catalytic activity under visible light, Catal. Lett. 125 (3) (2008) 320–330.
[62] A.J. Bard, L.R. Faulkner. Electrochemical Methods Fundamentals and Applications, Wiley, Newyork, NY, USA, 2001.
[63] R.S. Nicholson, Theory and application of cyclic voltammetry for measurement of electrode reaction kinetics, Anal. Chem. 37 (11) (1965) 1351–1355.
[64] E. Laviron, General expression of the linear potential sweep voltammogram in the case of diffusionless electrochemical systems, J. Electroanal. Chem. Interfacial Electrochem. 101 (1) (1979) 19–28.
[65] C. Kant, J. Deisenhofer, V. Tsurkan, A. Loidl, Magnetic susceptibility of the frustrated spinels $ZnC_{r2}O_4$, $MgCr_2O_4$ and $CdCr_2O_4$, J. Phys. Conf. Ser. 200 (3) (2010) 032032.
[66] E. Burello, A.P. Worth, A theoretical framework for predicting the oxidative stress potential of oxide nanoparticles, Nanotoxicology 5 (2) (2011) 228–235.
[67] E. Burello, A.P.QSAR Worth, Modeling of nanomaterials, WIREs Nanomed. Nanobiotechnology 3 (3) (2011) 298–306.